



HAL
open science

Nonlinear evolution of the centrifugal instability using a semi-linear model

Eunok Yim, P. Billant, F. Gallaire

► **To cite this version:**

Eunok Yim, P. Billant, F. Gallaire. Nonlinear evolution of the centrifugal instability using a semi-linear model. *Journal of Fluid Mechanics*, 2020. insu-03025061

HAL Id: insu-03025061

<https://insu.hal.science/insu-03025061>

Submitted on 26 Nov 2020

HAL is a multi-disciplinary open access archive for the deposit and dissemination of scientific research documents, whether they are published or not. The documents may come from teaching and research institutions in France or abroad, or from public or private research centers.

L'archive ouverte pluridisciplinaire **HAL**, est destinée au dépôt et à la diffusion de documents scientifiques de niveau recherche, publiés ou non, émanant des établissements d'enseignement et de recherche français ou étrangers, des laboratoires publics ou privés.

Nonlinear evolution of the centrifugal instability using a semi-linear model

Eunok Yim¹†, P. Billant² and F. Gallaire¹

¹LFMI, École Polytechnique Fédérale de Lausanne, 1015 Lausanne, Switzerland

²LadHyX, CNRS, École Polytechnique, F-91128 Palaiseau CEDEX, France

(Received xx; revised xx; accepted xx)

We study the nonlinear evolution of the axisymmetric centrifugal instability developing on a columnar anticyclone with a Gaussian angular velocity using a semi-linear approach. The model consists in two coupled equations: one for the linear evolution of the most unstable perturbation on the axially averaged mean flow and another for the evolution of the mean flow under the effect of the axially averaged Reynolds stresses due to the perturbation. Such model is similar to the self-consistent model of Mantič-Lugo *et al.* (2014) except that the time averaging is replaced by a spatial averaging. The non-linear evolutions of the mean flow and the perturbations predicted by this semi-linear model are in very good agreement with DNS for the Rossby number $Ro = -4$ and both values of the Reynolds numbers investigated: $Re = 800$ and 2000 (based on the initial maximum angular velocity and radius of the vortex). An improved model taking into account the second harmonic perturbations is also considered. The results show that the angular momentum of the mean flow is homogenized towards a centrifugally stable profile via the action of the Reynolds stresses of the fluctuations. The final velocity profile predicted by Kloosterziel *et al.* (2007) in the inviscid limit is extended to finite high Reynolds numbers. It is in good agreement with the numerical simulations.

Key words: Centrifugal instability, vortex, semi-linear model, stability analysis

1. Introduction

Centrifugal instability or inertial instability, is the most common instability developing on vortices in rotating medium. It is a local instability occurring when the balance between the centrifugal force and the pressure gradient is disrupted, i.e. when the square of the absolute angular momentum of the fluid decreases with radius r in inviscid fluids (Rayleigh 1917; Synge 1933; Kloosterziel & van Heijst 1991). While this condition applies to axisymmetric disturbances, a generalized criterion for non-axisymmetric perturbations has been derived by Billant & Gallaire (2005).

Linear stability analysis of a columnar vortex with Gaussian angular velocity in inviscid fluids shows that the growth rate is maximum at infinite wavenumber (Smyth & McWilliams 1998). However, as soon as viscous effects are taken into account, short wavelength are damped and the fastest growing mode has a finite wavenumber (Lazar *et al.* 2013; Yim *et al.* 2016).

Kloosterziel *et al.* (2007) and Carnevale *et al.* (2011) have analysed the nonlinear

† Email address for correspondence: eunok.yim@epfl.ch

evolution of the centrifugal instability in a rotating medium at high Reynolds number. They have shown that the vortex saturates to a centrifugally stable state where the Rayleigh instability condition is no longer satisfied, i.e. the square of the axial average of the absolute angular momentum does not decrease with radius. Hence, the instability redistributes the regions of positive and negative absolute angular momentum under the constraint of absolute angular momentum conservation in the inviscid limit.

The saturation of an instability towards a periodic limit cycle for which the mean flow is stable has been recently described by means of a self-consistent approach (Mantić-Lugo *et al.* 2014). In this approach, the flow is decomposed into time-averaged mean flow and unsteady perturbations. Then, the nonlinear saturation can be described by computing the mean flow distortion due to the Reynolds stresses of the perturbation and the linear growth of the perturbation on the mean flow. Here, we develop a similar approach for the centrifugal instability using a spatial average instead of a time average since the instability is spatially periodic but not periodic in time.

2. Governing equations

We consider the Carton & McWilliams vortex (Carton *et al.* 1989) with angular velocity (figure 1a)

$$\Omega = \Omega_0 \exp(-r^2/R^2), \quad (2.1)$$

where Ω_0 is the maximum angular velocity and R the radius of the vortex. Such isolated profile is frequently observed (Ioannou *et al.* 2017) and its stability has been extensively studied (Carton *et al.* 1989; Gent & McWilliams 1986; Smyth & McWilliams 1998; Billant & Gallaire 2005; Kloosterziel *et al.* 2007; Yim & Billant 2015). The vortex (2.1) is a steady solution of the Euler equation since it is axisymmetric and axially uniform. It is also an exact solution of the Navier-Stokes equation when Ω_0 and R are allowed to vary with time as follows: $\Omega_0 = \Omega_i (R_i/R)^4$ with $R^2 = R_i^2 + 4\nu t$, where ν is the kinematic viscosity and Ω_i , R_i are the initial angular velocity and radius. In the following, the length and time are non-dimensionalised with R and $1/\Omega_0$, respectively. The governing equations for the velocity field $\mathbf{u} = [u, v, w]$ in cylindrical coordinates (r, θ, z) read

$$\frac{\partial \mathbf{u}}{\partial t} + \mathbf{u} \cdot \nabla \mathbf{u} + 2Ro^{-1} \mathbf{e}_z \times \mathbf{u} = -\nabla p + Re^{-1} \nabla^2 \mathbf{u}, \quad (2.2)$$

$$\nabla \cdot \mathbf{u} = 0, \quad (2.3)$$

where the Reynolds and Rossby numbers are defined as $Re = \Omega_0 R^2 / \nu$ and $Ro = 2\Omega_0 / f$, respectively with f the Coriolis parameter. The divergence free condition (2.3) is not further written in the following sections but is always guaranteed.

2.1. Linear stability

The linear stability of the base flow (2.1) has been first studied by linearizing the equations (2.2)–(2.3) and assuming infinitesimal perturbations with axial wavenumber k , azimuthal wavenumber m and growth rate σ

$$[\tilde{\mathbf{u}}, \tilde{p}](r, \theta, z, t) = [\mathbf{u}, p](r) e^{\sigma t + ikz + im\theta} + c.c., \quad (2.4)$$

where *c.c.* indicates the complex conjugate and giving

$$\sigma \mathbf{u} + \mathcal{L}_{m,k}(\mathbf{u}_b) \mathbf{u} = 0, \quad (2.5)$$

where

$$\mathcal{L}_{m,k}(\mathbf{u}_b) \mathbf{u} \equiv \mathbf{u}_b \cdot \nabla_{m,k} \mathbf{u} + \mathbf{u} \cdot \nabla \mathbf{u}_b + 2Ro^{-1} \mathbf{e}_z \times \mathbf{u} + \nabla_{m,k} p - Re^{-1} \nabla_{m,k}^2 \mathbf{u}, \quad (2.6)$$

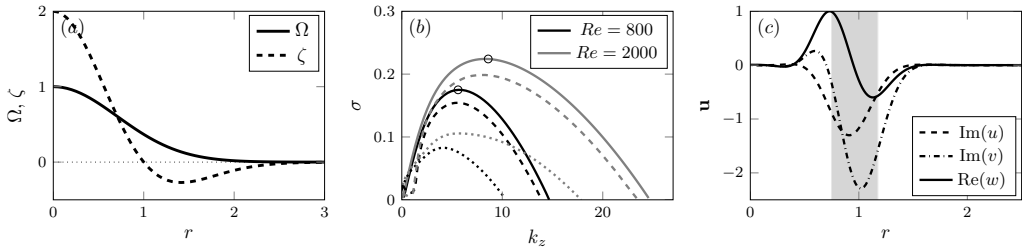


FIGURE 1. (a) Angular velocity (Ω) and axial vorticity (ζ) of the base flow. (b) Linear growth rate as a function of the vertical wavenumber k for different azimuthal wavenumbers: $m = 0$ (solid lines), $m = 1$ (dashed lines), $m = 2$ (dotted lines) for $Re = 800$ (black lines) and $Re = 2000$ (grey lines) for $Ro = -4$. The circles indicate the most unstable modes. (c) Most unstable eigenmode for $Re = 800$. The shaded area indicates the region where $\phi < 0$.

where $\mathbf{u}_b = [0, r\Omega, 0]$. Here, $\nabla_{m,k}$ and $\nabla_{m,k}^2$ are respectively the gradient and Laplacian in cylindrical coordinates with the azimuthal derivative replaced by im and the vertical derivative by ik .

In the inviscid limit, the necessary and sufficient condition for the instability of axisymmetric perturbations reads (Rayleigh 1917; Synge 1933; Kloosterziel & van Heijst 1991),

$$\phi = 2 \left(\frac{v}{r} + \frac{1}{Ro} \right) \left(\zeta + \frac{2}{Ro} \right) < 0. \quad (2.7)$$

For the base flow (2.1), (2.7) is satisfied when $Ro < -1$ or $Ro > \exp(2)$. Figure 1b shows the linear growth rate σ as a function of k for different azimuthal wavenumbers m for $Ro = -4$ for two different Reynolds numbers, $Re = 800$ and $Re = 2000$. The growth rate is maximum for the axisymmetric mode at $k_m = 5.6$ for $Re = 800$ and $k_m = 8.6$ for $Re = 2000$. As predicted by the generalized criterion of Billant & Gallaire (2005), only the first nonaxisymmetric modes $m = 1$ and $m = 2$ are unstable and their maximum growth rate is lower than for $m = 0$. Hence, in the following, we will focus on the axisymmetric mode at the most amplified vertical wavenumber k_m . Figure 1c shows the most unstable eigenmode for $Re = 800$, $Ro = -4$. It is mostly localized in the region where the Rayleigh discriminant is negative (shaded area).

3. Semi-linear formulation

We decompose the flow as

$$\mathbf{u}(r, \theta, z, t) = \bar{\mathbf{u}}(r, \theta, t) + \hat{\mathbf{u}}(r, \theta, z, t), \quad (3.1)$$

where $\bar{\mathbf{u}} = z_{\max}^{-1} \int_0^{z_{\max}} \mathbf{u} dz$ is the axially averaged mean flow and $\hat{\mathbf{u}}$ the perturbation which is not assumed to be small as in the linear stability analysis. Averaging the equation (2.2) in z leads to

$$\frac{\partial \bar{\mathbf{u}}}{\partial t} + \bar{\mathbf{u}} \cdot \nabla \bar{\mathbf{u}} + 2Ro^{-1} \mathbf{e}_z \times \bar{\mathbf{u}} + \nabla \bar{p} - Re^{-1} \nabla^2 \bar{\mathbf{u}} = -\overline{\hat{\mathbf{u}} \cdot \nabla \hat{\mathbf{u}}}. \quad (3.2)$$

Subtracting (3.2) from (2.2) yields the equation for the perturbation $\hat{\mathbf{u}}$,

$$\frac{\partial \hat{\mathbf{u}}}{\partial t} + \bar{\mathbf{u}} \cdot \nabla \hat{\mathbf{u}} + \hat{\mathbf{u}} \cdot \nabla \bar{\mathbf{u}} + 2Ro^{-1} \mathbf{e}_z \times \hat{\mathbf{u}} + \nabla \hat{p} - Re^{-1} \nabla^2 \hat{\mathbf{u}} = -\hat{\mathbf{u}} \cdot \nabla \hat{\mathbf{u}} + \overline{\hat{\mathbf{u}} \cdot \nabla \hat{\mathbf{u}}}. \quad (3.3)$$

These mean and fluctuation equations are similar to those of the Reynolds decomposition (Reynolds & Hussain 1972). They involve several coupling terms between the mean

and the fluctuation. The right hand side of (3.2) is the Reynolds stress due to the fluctuations which acts as forcing or added momentum to the nonlinear mean flow equation (left hand side of (3.2)). The amplitude of this forcing is proportional to the square of the fluctuation amplitude. In turn, the fluctuation in (3.3) is affected by the evolution of the mean flow through the advection operator $(\bar{\mathbf{u}} \cdot \nabla \hat{\mathbf{u}} + \hat{\mathbf{u}} \cdot \nabla \bar{\mathbf{u}})$. The fluctuation evolves also due to nonlinear effects with zero mean (right-hand side of 3.3) (Mantič-Lugo *et al.* (2014, 2015)).

3.1. Single harmonic

We introduce now the normal mode form of the perturbation for $m = 0$: $\hat{\mathbf{u}}(r, \theta, z, t) \equiv \hat{\mathbf{u}}(r, z, t) \simeq \mathbf{u}_1(r, t) \exp(ik_m z) + c.c.$ where k_m is the most amplified wavenumber obtained from the linear stability analysis. At $t = 0$, the perturbation is set as $\mathbf{u}_1(r, 0) = A_0 \mathbf{u}_m$ where \mathbf{u}_m is the dominant eigenmode and A_0 the initial amplitude of the perturbation. Neglecting the higher harmonics, the governing equations (3.2)-(3.3) reduce to

$$\frac{\partial \bar{\mathbf{u}}}{\partial t} + \bar{\mathbf{u}} \cdot \nabla \bar{\mathbf{u}} + 2Ro^{-1} \mathbf{e}_z \times \bar{\mathbf{u}} + \nabla \bar{p} - Re^{-1} \nabla^2 \bar{\mathbf{u}} = -\xi(\mathbf{u}_1), \quad (3.4)$$

$$\frac{\partial \mathbf{u}_1}{\partial t} + \mathcal{L}_{0,k}(\bar{\mathbf{u}}) \mathbf{u}_1 = 0, \quad (3.5)$$

where $\mathcal{L}_{0,k}(\bar{\mathbf{u}})$ is a linear operator defined in (2.6) with $m = 0$ and $\xi(\mathbf{u}_1) = \mathbf{u}_1 \cdot \nabla_{-k} \mathbf{u}_1^* + \mathbf{u}_1^* \cdot \nabla_k \mathbf{u}_1$ is the Reynolds stress. It is worth mentioning that (3.4) – (3.5) are now only a function of time and the radial coordinate r . In addition, the divergence free condition reduces to $1/r \partial r \bar{u} / \partial r = 0$ since $\partial \bar{w} / \partial z = 0$ due to the axial averaging. This implies $\bar{u} = 0$. It can also be shown that \bar{w} remains identically zero for all time if $\bar{w} = 0$ at $t = 0$, since the Reynolds stress in the z direction is zero. Thus, the mean flow has only a component along the azimuthal direction $\bar{\mathbf{u}} = [0, \bar{v}, 0]^T$. Hence, (3.4) simplifies to

$$\frac{\partial \bar{v}}{\partial t} = Re^{-1} \left[\frac{\partial^2 \bar{v}}{\partial r^2} + \frac{1}{r} \frac{\partial \bar{v}}{\partial r} - \frac{\bar{v}}{r^2} \right] - \xi(\mathbf{u}_1)_\theta, \quad (3.6)$$

which is a simple diffusion equation with a source term independent from the Rossby number Ro . Using the axisymmetry of the mean flow and of the perturbation, the linear equation (3.5) can be also further reduced to

$$\frac{\partial \eta_1}{\partial t} - \left(\frac{2\bar{v}}{r} + 2Ro^{-1} \right) ikv_1 - Re^{-1} \left[\frac{\partial^2 \eta_1}{\partial r^2} + \frac{1}{r} \frac{\partial \eta_1}{\partial r} - \frac{\eta_1}{r^2} - k^2 \eta_1 \right] = 0, \quad (3.7a)$$

$$\frac{\partial v_1}{\partial t} + (\bar{\zeta} + 2Ro^{-1}) u_1 - Re^{-1} \left[\frac{\partial^2 v_1}{\partial r^2} + \frac{1}{r} \frac{\partial v_1}{\partial r} - \frac{v_1}{r^2} - k^2 v_1 \right] = 0, \quad (3.7b)$$

where $\eta_1 = \partial_z u_1 - \partial_r w_1 = iku_1 - (i/kr) \partial_r ((1/r) \partial_r r u_1)$ is the azimuthal component of vorticity.

Therefore, our model consists in the semi-linear 1D equation (3.5), or equivalently (3.7), for the evolution of the perturbation over the mean flow coupled to the equation (3.6) for the evolution of the mean flow under the effects of the Reynolds stresses of the perturbation and viscous diffusion. The only difference compared to pure linear equations is this evolution of the mean flow. Such semi-linear model is similar to the self-consistent model proposed by Mantič-Lugo *et al.* (2014). The main difference is that the Reynolds decomposition (Reynolds & Hussain 1972) to separate the flow into a mean flow and a fluctuation is here based on spatial axial average since the perturbation is harmonic along the axis while the self-consistent model relies upon a time average because the perturbation is harmonic in time for the flows they have considered. Another difference

is that the perturbation equations are here simply integrated in time while, in the self-consistent model, an eigenvalue problem has to be solved after each variation of the mean flow.

3.2. Two harmonics

One can easily include higher harmonics of the fundamental mode following the same approach. For instance, taking into account the second harmonic in the velocity perturbation: $\hat{\mathbf{u}} = \mathbf{u}_1(r)\exp(ik_m z) + \mathbf{u}_2(r)\exp(i2k_m z) + c.c.$, the perturbation equations become

$$\frac{\partial \mathbf{u}_1}{\partial t} + \mathcal{L}_{0,k}(\bar{\mathbf{u}})\mathbf{u}_1 = -(\mathbf{u}_2 \cdot \nabla_{-k}\mathbf{u}_1^* + \mathbf{u}_1^* \cdot \nabla_{2k}\mathbf{u}_2), \quad (3.8a)$$

$$\frac{\partial \mathbf{u}_2}{\partial t} + \mathcal{L}_{0,2k}(\bar{\mathbf{u}})\mathbf{u}_2 = -(\mathbf{u}_1 \cdot \nabla_k\mathbf{u}_1). \quad (3.8b)$$

The mean flow (3.6) is then forced by the Reynolds stress of both harmonics

$$\frac{\partial \bar{v}}{\partial t} = Re^{-1} \left[\frac{\partial^2 \bar{v}}{\partial r^2} + \frac{1}{r} \frac{\partial \bar{v}}{\partial r} - \frac{\bar{v}}{r^2} \right] - \xi(\mathbf{u}_1)_\theta - \xi(\mathbf{u}_2)_\theta. \quad (3.9)$$

Higher harmonics $3k_m, 4k_m, \dots$ can be taken into account similarly. Since the perturbations equation are integrated in time, there is no particular complexity arising when several harmonics are considered. This is in contrast with the self-consistent model (Mantič-Lugo *et al.* 2014) where the eigenvalue problems become increasingly complicated when more than one harmonic is considered (Meliga 2017).

3.3. Numerical method

The semi-linear numerical simulations have been performed with the FreeFEM++ software (Hecht 2012) for axisymmetric cylindrical coordinates (r, z) . The velocity and pressure of equations (2.2)–(2.3) are discretised with Taylor-Hood P2 and P1 elements, respectively. The time is discretised using the first order backward Euler formula. The total numbers of degree of freedom is 4687. Three-dimensional (3D) DNS have been performed using the open source spectral element code Nek5000 (Fischer *et al.* 2008) in Cartesian coordinates (x, y, z) in cylindrical geometry. The domain is discretized by 120000 hexahedral elements and each element is composed with 8 (velocity) or 6 (pressure) Gauss-Lobatto-Legendre quadrature points along each direction (resulting in 250 million degrees of freedom, i.e. 50000 times more than for the semi-linear models). The time and the nonlinear convection terms are discretised using third order backward differentiation and third order explicit extrapolation formula, respectively.

Both DNS and semi-linear models are initialized with the perturbation $\hat{\mathbf{u}} = A_0 \mathbf{u}_m \exp(ik_m z) + c.c.$ where $A_0 = 0.001$ is the initial amplitude and \mathbf{u}_m is the most unstable linear eigenmode (figure 1c) obtained by means of the restarted Arnoldi method. The eigenmodes have been normalized so that the absolute maximum value of the vertical velocity is unity, $\max(|w_m|) = 1$ such that $\max(|\hat{w}|) = A_0$.

The domain size for the semi-linear model is chosen to be $r = [0, r_{\max}]$ where $r_{\max} = 8$. Since the base angular velocity decays exponentially with r^2 , the radial extent does not need to be large: the eigenvalues and eigenvectors are converged as soon as $r_{\max} > 5$. Periodic boundary conditions are applied on $z = 0$ and $z = z_{\max}$. The boundary conditions at $r = 0$ are $u = v = 0$ since the flow is axisymmetric (Batchelor & Gill 1962). At $r = r_{\max}$, all perturbations are enforced to vanish. The domain sizes in the DNS are $r = [-8, 8]$ along the horizontal with no slip boundary conditions and $z = [0, 13 \cdot 2\pi/k_m]$ along the vertical with periodic boundary conditions. To validate the numerical methods,

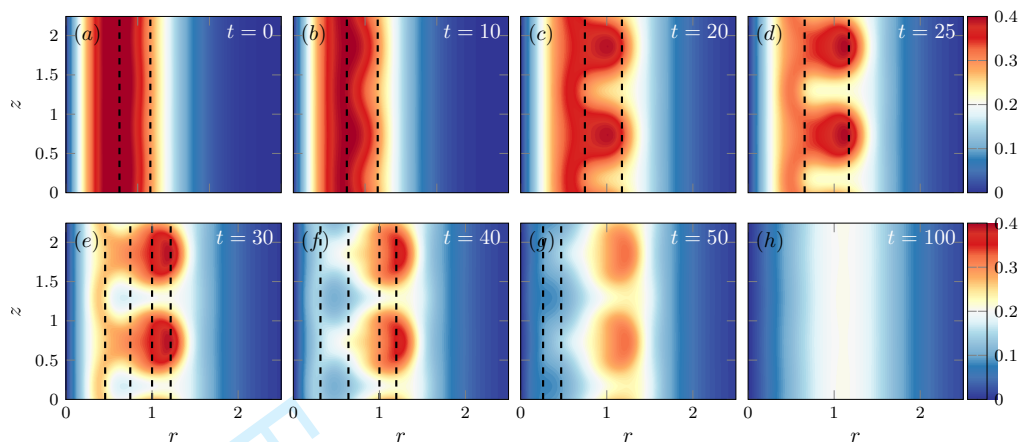


FIGURE 2. Vertical cross-sections at $x = 0$ of the evolution of the azimuthal velocity field v in DNS for $k_m = 5.6$, $Ro = -4$, $Re = 800$. The dashed lines delimit the regions where $\bar{\phi} < 0$ based on the mean azimuthal velocity \bar{v} . Only two wavelengths are shown whereas the full domain contains 13 wavelengths along the vertical (see §3.3).

some DNS and simulations with the semi-linear models have been also performed with an independent pseudo-spectral code NS3D (Deloncle *et al.* 2008). Identical results have been obtained.

4. Results

We consider a single Rossby number $Ro = -4$. This value has been chosen to be sufficiently far from the marginal stability limit $Ro = -1$ so that the initial growth rate and non-linear effects are not weak. In other words, we are not in a weakly nonlinear regime as assumed to derive asymptotically amplitude equations. Two Reynolds numbers will be investigated: $Re = 800$ and $Re = 2000$ corresponding to different viscous damping and, thus, to different values of the initial growth rates (figure 1b). This allows us to test the semi-linear models for two representative cases where nonlinear effects and higher harmonics are expected to be moderate ($Re = 800$) or more important ($Re = 2000$). Alternatively, different growth rates could have been obtained by varying Ro with Re fixed.

4.1. 3D DNS

Figure 2 shows snapshots of the azimuthal velocity v in a DNS for $Ro = -4$ and $Re = 800$. Only two wavelengths are displayed although the computation is performed over 13 wavelengths. The vertical lines delimit the regions where the Rayleigh discriminant $\bar{\phi}$ is negative, where $\bar{\phi}$ is based on the axially averaged azimuthal velocity $\bar{v}(t, r)$. At $t = 10$, a slight deformation can be seen in the region where $\bar{\phi} < 0$. Subsequently, the perturbation grows and rearranges the distribution of azimuthal velocity ($20 < t < 30$). For $t > 30$, the ‘mushrooms’ start to fade out. Finally, vertical deformations are no longer visible by $t = 100$ so that the vortex then evolves only by viscous diffusion.

The solid lines in figure 3a show the evolution of the corresponding mean azimuthal velocity \bar{v} . The mean flow profile first decays by viscous diffusion until $t = 10$. A distortion of the mean flow due to the instability can be seen at $t = 20$. At $t = 30$ and $t = 40$, it becomes strong and the profile exhibits two distinct peaks near $r = 0.4$ and $r = 1$. Then, the peak at $r \sim 0.4$ disappears and the mean azimuthal velocity profile becomes linear

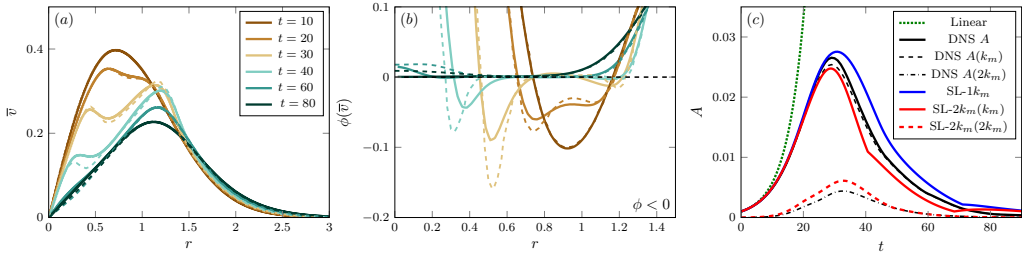


FIGURE 3. (a) Mean azimuthal velocity \bar{v} from DNS (solid lines) and SL- $1k_m$ model (dashed lines), (b) corresponding Rayleigh discriminant $\bar{\phi}$ and (c) perturbation amplitudes A as a function of time for $Ro = -4$ and $Re = 800$.

for $r < 1$ for $t > 60$. During this process, the maximum velocity has decreased from $\max(\bar{v}(t = 0)) = 0.47$ to $\max(\bar{v}(t = 80)) = 0.23$ and the corresponding radius has moved from $r = 0.7$ to $r = 1.2$. The corresponding Rayleigh discriminant is shown in figure 3b (solid lines). At $t = 0$, $\bar{\phi}$ is minimum at $r = 0.95$ and is negative for $0.75 < r < 1.18$. For $t = 20$, the region where $\bar{\phi} < 0$ has enlarged but the minimum of $\bar{\phi}$ has decreased in absolute value. At $t = 30$, there exist two regions where $\bar{\phi} < 0$: near $r = 0.3$ and $r = 0.8$ while $\bar{\phi} > 0$ in between. The minimum value decreases and then increases again for larger time. By comparing figure 3a and figure 3b, we can see that the mean flow is mostly deformed near the negative peaks of $\bar{\phi}$ at least until $t = 40$. At $t = 60$, $\min(\bar{\phi})$ is no longer negative.

The evolution of the instability is qualitatively similar for the higher Reynolds number $Re = 2000$. (figure 4). For this DNS, full vertical cross-sections of the azimuthal velocity and horizontal cross-sections of the vertical velocity are displayed at three selected times. As can be seen, the flow seems to remain axisymmetric and no subharmonic modulations of the primary wavelength are visible along the vertical. This is confirmed quantitatively in figure 5a,b which shows the averaged azimuthal $\overline{P_\theta(m, t)}$ and axial $\overline{P_z(k, t)}$ Fourier spectra defined as

$$\overline{P_\theta(m, t)} = \frac{1}{r_{\max} z_{\max}} \int_0^{r_{\max}} \int_0^{z_{\max}} FT_\theta[w(r, \theta, z, t)] FT_\theta^*[w(r, \theta, z, t)] dz dr, \quad (4.1)$$

$$\overline{P_z(k, t)} = \frac{1}{r_{\max}} \int_0^{r_{\max}} FT_z[w(r, [0, \pi], z, t)] FT_z^*[w(r, [0, \pi], z, t)] dr, \quad (4.2)$$

where $FT_\theta[w(r, \theta, z, t)]$ and $FT_z[w(r, \theta, z, t)]$ are the azimuthal and axial Fourier transforms of the axial velocity w . The axisymmetric $m = 0$ mode remains always largely dominant (figure 5a) and only the fundamental mode k_m and higher harmonics grows significantly (figure 5b). This legitimates the assumptions behind the semi-linear models where only the most amplified axisymmetric mode, and possibly higher vertical harmonics, are taken into account.

The evolution of the mean azimuthal velocity \bar{v} for $Re = 2000$ (solid lines in figure 6a) resembles the one for the lower Reynolds $Re = 800$ (figure 3). The deformations at intermediate times are nevertheless more pronounced for $Re = 2000$.

4.2. SL- $1k_m$ semi-linear model

The dashed lines in figure 3a represent the mean azimuthal flow predicted by the semi-linear model with one harmonic, abbreviated as SL- $1k_m$, for $Re = 800$. The agreement with the DNS is almost perfect for $t = 10, 20$ while some discrepancies can be seen at $t = 30, 40$. It becomes excellent again for $t > 60$. Similar agreement and discrepancies are

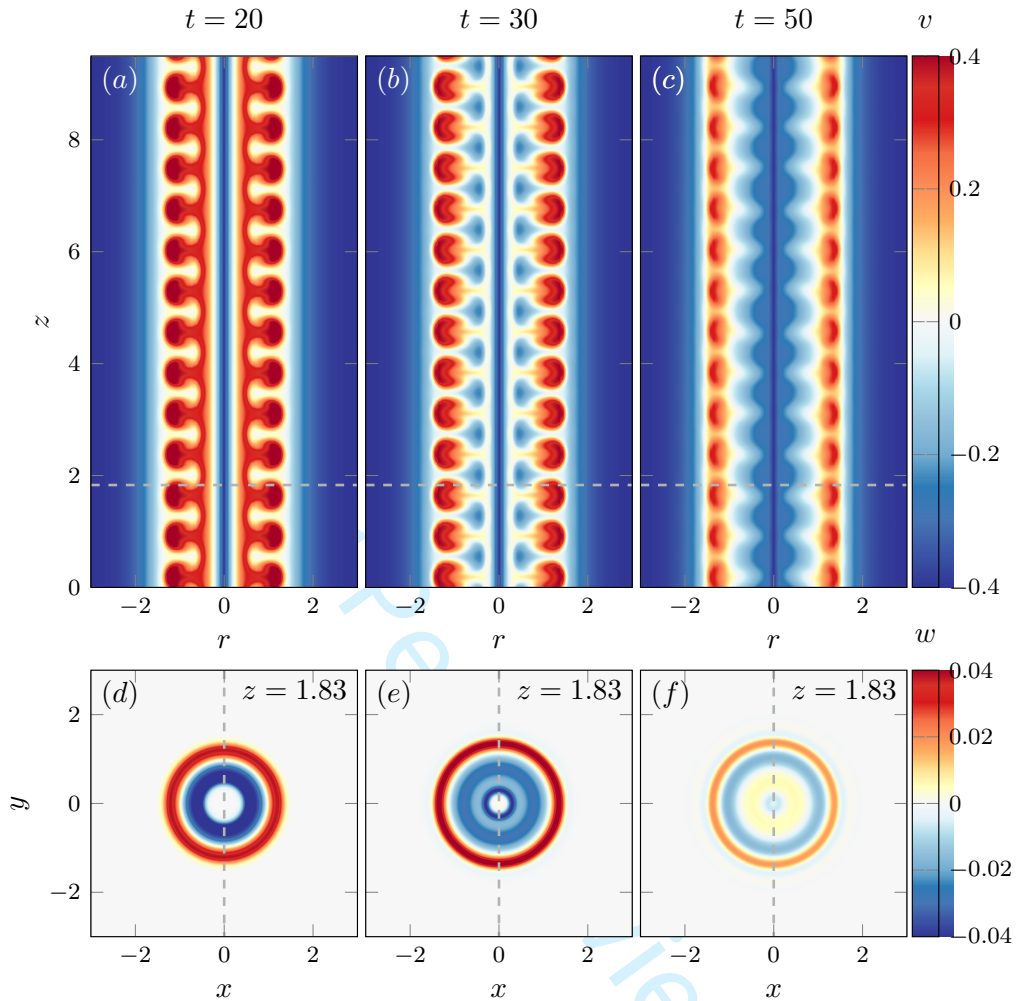


FIGURE 4. Evolution of the azimuthal velocity (*a, b, c*) and axial velocity (*d, e, f*) in a DNS for $k_m = 8.6$, $Ro = -4$, $Re = 2000$. (*a, d*) $t = 20$, (*b, e*) $t = 30$ and (*c, f*) $t = 50$. The vertical cross-sections (*a, b, c*) are at $x = 0$ and the horizontal cross-sections (*d, e, f*) at $z = 1.83$. The location of the different cross-sections are indicated by the dashed lines.

also observed for the Rayleigh discriminant $\bar{\phi}$ (figure 3b). Figure 3c shows the amplitude of the velocity perturbation $A = \max(|w|)$, in the DNS (black solid line) and the semi-linear model. The amplitude first increases exponentially from its initial value $A_0 = 0.001$. The linear prediction (dotted line) agrees with the DNS only for small time ($t < 10$). Then, the growth rate becomes smaller than the linear growth rate. The perturbation grows until $t = 30$ and then decreases. The amplitude of the first and second harmonics $A(k_m)$, $A(2k_m)$ have been decomposed using FFT (broken lines). The amplitude of the second harmonic is around 15% of the amplitude of the first harmonic. The amplitude of the perturbation in the semi-linear model SL- $1k_m$ (blue thick line) is in very good agreement with the one in the DNS until $t = 30$. Then, it slightly overestimates the amplitude extracted from the DNS.

For the higher Reynolds number $Re = 2000$, the evolution of the mean azimuthal flow and amplitudes of the perturbation in the DNS and SL- $1k_m$ model are also globally in

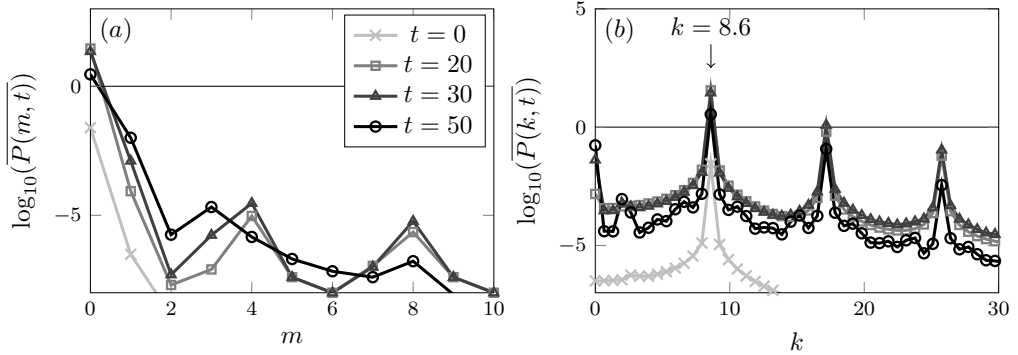


FIGURE 5. (a) Axially averaged azimuthal spectral amplitude $\overline{P_\theta(m,t)}$ and (b) radially averaged axial spectral amplitude, $\overline{P_z(k,t)}$ of axial velocity w for times $t = 0, 20, 30$ and 50 for $Re = 2000, Ro = -4$.

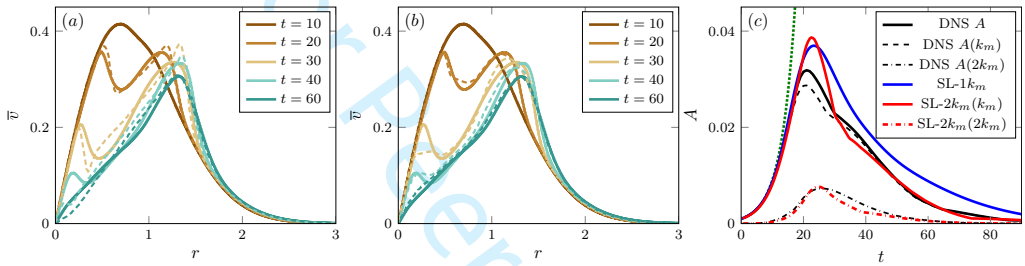


FIGURE 6. (a) Mean azimuthal velocity from DNS (solid lines) and semi-linear model SL- $1k_m$ (dashed lines) and (b) for SL- $2k_m$ (dashed lines). (c) The perturbation amplitudes A as a function of time for $Ro = -4$ and $Re = 2000$ for both SL- $1k_m$ and SL- $2k_m$.

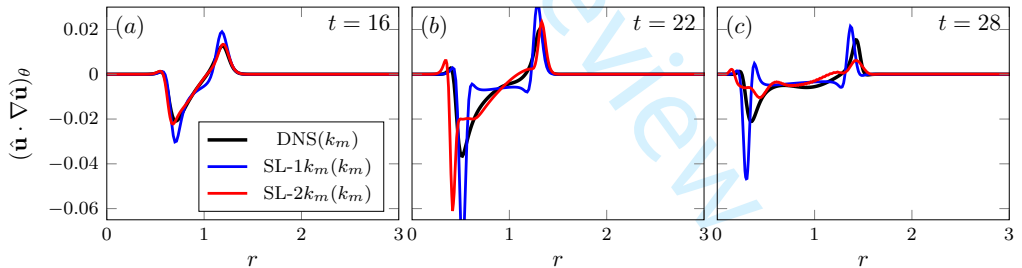


FIGURE 7. Mean Reynolds stresses in the azimuthal direction from DNS and semi-linear models at (a) $t = 16$, (b) $t = 22$ and (c) $t = 28$.

good agreement (figure 6a,c). Nevertheless, some deviations can be seen at $t = 30, 40$, in particular the first peak at small radius is not captured at $t = 40$. In addition, the maximum amplitude of the second harmonic reaches 1/3 of the maximum amplitude of the fundamental harmonic (figure 6c).

4.3. SL- $2k_m$ semi-linear model

As seen in figures 3c and 6c, the second harmonic is triggered and reaches a non-negligible amplitude for both $Re = 800$ and $Re = 2000$. Its effect can be taken into account by means of the semi-linear model (3.8-3.9), called SL- $2k_m$. Since the perturbation is initialized by only the leading eigenmode, the initial amplitude of the

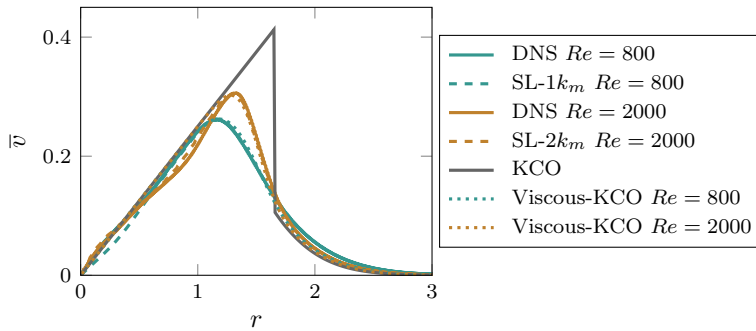


FIGURE 8. Mean azimuthal velocity in the DNS and semi-linear models at $t = 60$ for $Ro = -4$ for $Re = 800$ and $Re = 2000$. KCO indicates the velocity distribution predicted by Kloosterziel *et al.* (2007) in the inviscid limit. Viscous-KCO corresponds to the velocity profile (5.11) which takes into account viscous effects.

second harmonic is set to zero. Therefore, even if it is also unstable (figure 1b), its initial evolution is only due to the forcing by the fundamental harmonic.

For $Re = 800$ (figure 3c), the evolution of the amplitude of the first harmonic predicted by the SL- $2k_m$ model (red continuous line) is slightly closer to the amplitude $A(k_m)$ in the DNS (black dashed line) than for the SL- $1k_m$ model (blue continuous line). However, for $Re = 2000$ (figure 6c), the SL- $2k_m(k_m)$ amplitude is not closer to $A(k_m)$ in the DNS than the SL- $1k_m$ model for $20 \lesssim t \lesssim 30$. The amplitudes of the second harmonic are also well predicted by the SL- $2k_m$ model. It reaches 15% and 26% of the amplitude of the fundamental harmonic for $Re = 800$ and $Re = 2000$, respectively.

For $Re = 2000$, the predicted profiles for the mean azimuthal velocity for the SL- $2k_m$ model (figure 6b) are smoother than for the SL- $1k_m$ model (figure 6a). However, the first peak near $r \sim 0.3$ at $t = 30$ is less pronounced. To understand this discrepancy, we have plotted the Reynolds stresses in the θ -direction in the DNS and the semi-linear models (figure 7). At $t = 16$, the SL- $2k_m$ model is in excellent agreement with the DNS, while at $t = 22$ and $t = 28$, there are some departures especially at small radius ($r \approx 0.5$). This is the reason why the SL- $2k_m$ model does not capture the first peak of the mean azimuthal velocity (figure 6b).

Including higher harmonics might further improve the predictions. However, this would complicate the models while the primary goal of the present approach is the simplicity rather than the accuracy.

5. Final profiles of azimuthal velocity

The profiles of mean azimuthal velocity observed at late time $t = 60$, once the instability has ceased, have been compared to the theory of Kloosterziel *et al.* (2007) and Carnevale *et al.* (2011). As mentioned in the introduction, this theory states that the centrifugal instability homogenizes negative and positive absolute angular momentum $L = r(v+r/Ro)$ so as to suppress negative gradients of L^2 under the constraint of absolute angular momentum conservation. For anticyclones, the final profile of L in the inviscid limit is such that L is zero until a radius r_c given by $\int_0^{r_c} rL_i dr = 0$, where L_i is the initial absolute angular momentum. Beyond this radius, the velocity profile remains identical to the initial one. Therefore, the theoretical angular velocity is

$$\Omega(r < r_c) = -\frac{1}{Ro}, \quad \Omega(r \geq r_c) = \exp(-r^2). \quad (5.1)$$

This profile (labelled KCO) is compared to those observed in the DNS and SL models for $Re = 800$ and $Re = 2000$ in figure 8. It is close to the observed profiles except in the vicinity of the radius r_c where the latter are smooth while the theoretical profile is discontinuous due to the inviscid approximation. In order to take into account viscous effects, we have further considered the viscous diffusion of (5.1). For large Reynolds number, the diffusion equation

$$\frac{\partial \Omega}{\partial t} = Re^{-1} \left[\frac{\partial^2 \Omega}{\partial r^2} + \frac{3}{r} \frac{\partial \Omega}{\partial r} \right]. \quad (5.2)$$

shows that the angular velocity should decay slowly everywhere except in the vicinity of r_c where radial derivatives are expected to be large because of the discontinuity. To describe the local viscous evolution near r_c , we therefore define a rescaled radial coordinate $\tilde{r} = \sqrt{Re}(r - r_c)$ and we assume that Ω depends both on \tilde{r} and the unscaled radius r . We also introduce a slow time $\tau = Re^{-1}t$. Hence, (5.2) becomes

$$\frac{\partial \Omega}{\partial t} + \frac{1}{Re} \frac{\partial \Omega}{\partial \tau} = \frac{\partial^2 \Omega}{\partial \tilde{r}^2} + \frac{1}{\sqrt{Re}} \left(2 \frac{\partial^2 \Omega}{\partial \tilde{r} \partial r} + \frac{3}{r} \frac{\partial \Omega}{\partial \tilde{r}} \right) + \frac{1}{Re} \left(\frac{\partial^2 \Omega}{\partial r^2} + \frac{3}{r} \frac{\partial \Omega}{\partial r} \right). \quad (5.3)$$

Then, the solution is sought as an expansion in Reynolds number

$$\Omega = \Omega_0 + Re^{-1/2} \Omega_1 + Re^{-1} \Omega_2 + \dots \quad (5.4)$$

The zero-th and first order problems are

$$\frac{\partial \Omega_0}{\partial t} = \frac{\partial^2 \Omega_0}{\partial \tilde{r}^2}, \quad \text{and} \quad \frac{\partial \Omega_1}{\partial t} - \frac{\partial^2 \Omega_1}{\partial \tilde{r}^2} = 2 \frac{\partial^2 \Omega_0}{\partial \tilde{r} \partial r} + \frac{3}{r} \frac{\partial \Omega_0}{\partial \tilde{r}}. \quad (5.5)$$

The solutions are chosen as

$$\Omega_0 = A(r, \tau) \operatorname{erf} \left(\frac{\tilde{r}}{2\sqrt{t}} \right) + H(r, \tau), \quad \text{and} \quad \Omega_1 = \left(2 \frac{\partial A}{\partial r} + 3 \frac{A}{r} \right) \sqrt{\frac{t}{\pi}} \exp \left(-\frac{\tilde{r}^2}{4t} \right). \quad (5.6)$$

where A and H are arbitrary functions of r and τ . These functions are found by considering the problem at order Re^{-1} :

$$\frac{\partial \Omega_2}{\partial t} - \frac{\partial^2 \Omega_2}{\partial \tilde{r}^2} = -\frac{\partial \Omega_0}{\partial \tau} + \frac{\partial^2 \Omega_0}{\partial r^2} + \frac{3}{r} \frac{\partial \Omega_0}{\partial r} + 2 \frac{\partial^2 \Omega_1}{\partial r \partial \tilde{r}} + \frac{3}{r} \frac{\partial \Omega_1}{\partial \tilde{r}}. \quad (5.7)$$

It can be shown that the solution Ω_2 presents secular growth unless we set

$$\frac{\partial A}{\partial \tau} = \frac{\partial^2 A}{\partial r^2} + \frac{3}{r} \frac{\partial A}{\partial r}, \quad \text{and} \quad \frac{\partial H}{\partial \tau} = \frac{\partial^2 H}{\partial r^2} + \frac{3}{r} \frac{\partial H}{\partial r}. \quad (5.8)$$

The solutions are taken as

$$A = \frac{D \exp \left(-\frac{r^2}{B+4\tau} \right)}{(B+4\tau)^2} + C, \quad \text{and} \quad H = \frac{E \exp \left(-\frac{r^2}{G+4\tau} \right)}{(G+4\tau)^2} + F, \quad (5.9)$$

where B, C, D, E, F and G are constants. We then impose that Ω_0 at $t = \tau = 0$ matches the profile (5.1). This implies $B = G = 1$, $E = D = 1/2$, $F = -C = -1/(2Ro)$. Then, the solution of (5.7) can be found

$$\Omega_2 = -\frac{1}{\sqrt{\pi}} \left(\frac{\partial^2 A}{\partial r^2} + \frac{3}{r} \frac{\partial A}{\partial r} + \frac{3}{4r^2} A \right) \tilde{r} \sqrt{t} \exp \left(-\frac{\tilde{r}^2}{4t} \right). \quad (5.10)$$

Finally, the complete solution for Ω up to order Re^{-1} , written back in terms of the original variables r and t , reads

$$\Omega = A \operatorname{erf} \left(\frac{\sqrt{Re}(r - r_c)}{2\sqrt{t}} \right) + A - \frac{1}{Ro} + \left[2 \frac{\partial A}{\partial r} + \frac{3}{r} A - \left(\frac{\partial^2 A}{\partial r^2} + \frac{3}{r} \frac{\partial A}{\partial r} + \frac{3}{4r^2} A \right) (r - r_c) \right] \sqrt{\frac{t}{\pi Re}} \exp \left(-\frac{Re(r - r_c)^2}{4t} \right), \quad (5.11)$$

where A is given by (5.9) with the substitution $r = r$ and $\tau = Re^{-1}t$. The azimuthal velocity profiles corresponding to (5.11) are plotted with dotted lines (viscous-KCO) in figure 8. The time in (5.11) has not been set to $t = 60$ but to $t = 20$. Indeed, since the profile (5.1) is the outcome of the centrifugal instability, we have assumed that it is virtually formed only at $t = 40$ once the instability has almost ceased. These viscous profiles are in much better agreement with the DNS than the inviscid profile of Kloosterziel *et al.* (2007) and Carnevale *et al.* (2011). Besides, we emphasize that the profiles in the DNS and SL models are in excellent agreement.

6. Conclusion

We have studied the nonlinear growth of the centrifugal instability in an anticyclone with Gaussian angular velocity in rotating fluids for $Ro = -4$. We have used an approach similar to the one behind the self-consistent model (Mantič-Lugo *et al.* 2014). Using Reynolds decompositions (Reynolds & Hussain 1972) based upon a time average, Mantič-Lugo *et al.* (2014) have separated the flow into mean flow and time harmonic fluctuations. These two components are coupled via Reynolds stresses in the mean flow equation and via the evolution of the mean flow in the fluctuation equation. In the present study on the centrifugal instability, we have used a spatial average instead of a time average and separated the flow into axially averaged mean flow and spatial harmonic fluctuation. Like for the self-consistent model, the fluctuation grows over an evolving mean flow while the mean flow is forced by the Reynolds stresses due to the fluctuations. They contribute to the progressive smoothing of the destabilizing vorticity, thereby reducing the instantaneous growth of disturbances. A similar saturating or stabilizing effect is encountered in supercritical instabilities like vortex shedding behind a cylinder and flow over a cavity, although the Reynolds stresses can also be further destabilizing in subcritical flows like wall-bounded shear flows. The present semi-linear model with one harmonic is in very good agreement with DNS for $Re = 800$ and $Re = 2000$ concerning both the time evolution of the fluctuation amplitude and of the mean flow profiles. Including a second harmonic $2k_m$ into the model improves slightly the predictions.

We have also compared the ‘final’ azimuthal velocity profile observed in the DNS and semi-linear models when the instability has disappeared to the inviscid profile proposed by Kloosterziel *et al.* (2007) based on homogenization of angular momentum towards a centrifugally stable flow. They agree except in the neighbourhood of the radius where the inviscid profile is discontinuous. To improve the prediction, we have computed asymptotically for large Reynolds number the viscous diffusion of the theoretical profile of Kloosterziel *et al.* (2007). The discontinuity is then smoothed and the predicted profiles are in much better agreement with the profile observed in the DNS and semi-linear models.

The main interest of the present semi-linear models is their simplicity which may enable a deeper understanding of the underlying physics. In addition, we emphasize that they are very cheap in terms of computational cost. Indeed, the computing time for the present

3D DNS with the Nek5000 code takes 18 hours (elapsed real time) with 168 processors for 13 vertical wavelengths and for 100 time units. In contrast, a run of the semi-linear model with one or two harmonics only takes 6min or 10min, respectively with a single processor. This dramatic decrease on the computing time comes from the reduction of the problem to only few one-dimensional equations.

In the future, it would be interesting to investigate the connection between semi-linear models and amplitude equations derived from weakly nonlinear analyses. In addition, it would be interesting to develop similar models for non-axisymmetric centrifugal instabilities since they can be dominant in presence of background stratification (Lahaye & Zeitlin 2015; Yim *et al.* 2016, 2019). A similar approach could be also attempted for the two-dimensional shear instability by means of an azimuthal average.

Declaration of Interests. The authors report no conflict of interest.

REFERENCES

- BATCHELOR, G. K. & GILL, A. E. 1962 Analysis of the stability of axisymmetric jets. *J. Fluid Mech.* **14** (4), 529–551.
- BILLANT, P. & GALLAIRE, F. 2005 Generalized rayleigh criterion for non-axisymmetric centrifugal instabilities. *J. Fluid Mech.* **542**, 365–379.
- CARNEVALE, G. F., KLOOSTERZIEL, R. C., ORLANDI, P. & VAN SOMMEREN, D. D. J. A. 2011 Predicting the aftermath of vortex breakup in rotating flow. *J. Fluid Mech.* **669**, 90–119.
- CARTON, X., FLIERL, G. R. & POLVANI, L. M. 1989 The generation of tripoles from unstable axisymmetric isolated vortex structures. *EPL (Europhysics Letters)* **9** (4), 339.
- DELONCLE, A., BILLANT, P. & CHOMAZ, J.-M. 2008 Nonlinear evolution of the zigzag instability in stratified fluids: a shortcut on the route to dissipation. *J. Fluid Mech.* **599**, 229–239.
- FISCHER, P. F., LOTTES, J. W. & KERKEMEIER, S. G. 2008 Nek5000 Web page. <http://nek5000.mcs.anl.gov>.
- GENT, P. R. & MCWILLIAMS, J. C. 1986 The instability of barotropic circular vortices. *Geophys. Astrophys. Fluid Dyn.* **35** (1-4), 209–233.
- HECHT, F. 2012 New development in freefem++. *J. Numer. Math.* **20** (3-4), 251–265.
- IOANNOU, A., STEGNER, A., LE VU, B., TAUPIER-LETAGE, I. & SPEICH, S. 2017 Dynamical evolution of intense irapetra eddies on a 22 year long period. *J. Geophys. Res.* **122** (11), 9276–9298.
- KLOOSTERZIEL, R. C., CARNEVALE, G. F. & ORLANDI, P. 2007 Inertial instability in rotating and stratified fluids: barotropic vortices. *J. Fluid Mech.* **583**, 379–412.
- KLOOSTERZIEL, R. C. & VAN HEIJST, G. J. F. 1991 An experimental study of unstable barotropic vortices in a rotating fluid. *J. Fluid Mech.* **223**, 1–24.
- LAHAYE, N. & ZEITLIN, V. 2015 Centrifugal, barotropic and baroclinic instabilities of isolated ageostrophic anticyclones in the two-layer rotating shallow water model and their nonlinear saturation. *J. Fluid Mech.* **762**, 5–34.
- LAZAR, A., STEGNER, A. & HEIFETZ, E. 2013 Inertial instability of intense stratified anticyclones. part 1. generalized stability criterion. *J. Fluid Mech.* **732**, 457–484.
- MANTIĆ-LUGO, V., C., ARRATIA, C. & GALLAIRE, F. 2014 Self-consistent mean flow description of the nonlinear saturation of the vortex shedding in the cylinder wake. *Phys. Rev. Lett.* **113**, 084501.
- MANTIĆ-LUGO, V., C., ARRATIA, C. & GALLAIRE, F. 2015 A self-consistent model for the saturation dynamics of the vortex shedding around the mean flow in the unstable cylinder wake. *Phys. Fluids* **27** (7), 074103.
- MELIGA, P. 2017 Harmonics generation and the mechanics of saturation in flow over an open cavity: a second-order self-consistent description. *J. Fluid Mech.* **826**, 503–521.
- RAYLEIGH, LORD 1917 On the dynamics of revolving fluids. *Proc. R. Soc. A* **93** (648), 148–154.
- REYNOLDS, W. C. & HUSSAIN, A. K. M. F. 1972 The mechanics of an organized wave in turbulent shear flow. part 3. theoretical models and comparisons with experiments. *J. Fluid Mech.* **54** (2), 263–288.

- SMYTH, W. D. & MCWILLIAMS, J. C. 1998 Instability of an axisymmetric vortex in a stably stratified, rotating environment. *Theor. Comp. Fluid Dyn.* **11** (3-4), 305–322.
- SYNGE, J. L. 1933 The stability of heterogeneous liquids. *Trans. R. Soc. Canada* **27**, 1.
- YIM, E. & BILLANT, P. 2015 On the mechanism of the gent–mcwilliams instability of a columnar vortex in stratified rotating fluids. *J. Fluid Mech.* **780**, 5–44.
- YIM, E., BILLANT, P. & MÉNESGUEN, C. 2016 Stability of an isolated pancake vortex in continuously stratified-rotating fluids. *J. Fluid Mech.* **801**, 508–553.
- YIM, E., STEGNER, A. & BILLANT, P. 2019 Stability criterion for the centrifugal instability of surface intensified anticyclones. *J. Phys. Oceanogr.* **49** (3), 827–849.

For Peer Review